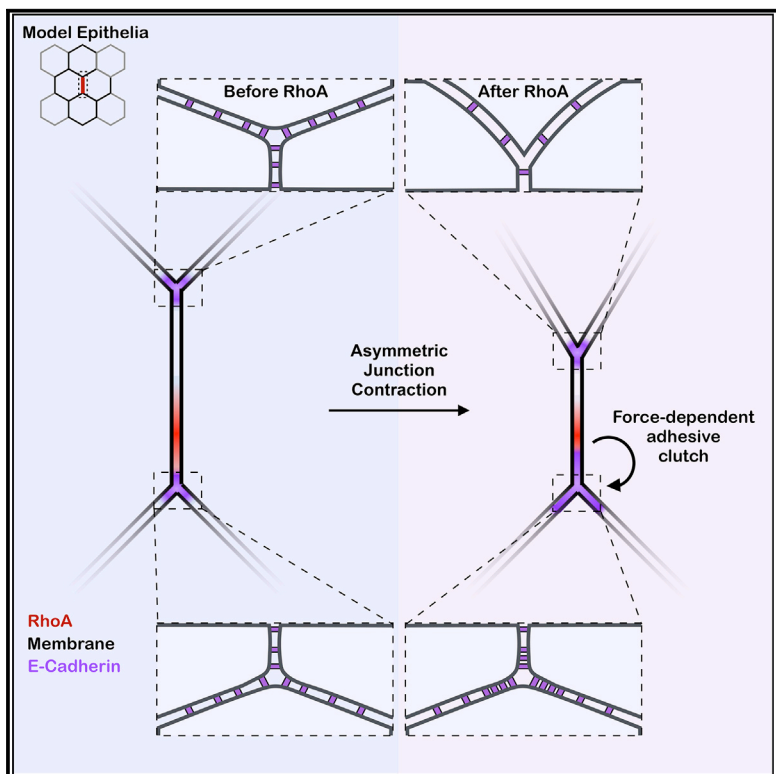


## Force-dependent intercellular adhesion strengthening underlies asymmetric adherens junction contraction

### Graphical abstract



### Authors

Kate E. Cavanaugh,  
Michael F. Staddon,  
Theresa A. Chmiel, ..., Alpha S. Yap,  
Shiladitya Banerjee, Margaret L. Gardel

Correspondence  
gardel@uchicago.edu

### In brief

Cavanaugh et al. use optogenetic control of RhoA in model epithelia and biophysical modeling to reveal a force-dependent intercellular clutch acting at tricellular vertices anchoring cell-cell junctions. RhoA mediates a force-sensitive E-cadherin adhesion strengthening to generate asymmetries in vertex motion which underlie junction contractions.

### Highlights

- Heterogeneous RhoA drives asymmetries in vertex motion during junction contractions
- Mechanosensitive E-cadherin induces friction to stabilize tricellular vertices
- Tension modulates friction and stiffness to induce vertex asymmetry
- Tricellular vertices act as molecular clutches upon RhoA-mediated force production



## Article

# Force-dependent intercellular adhesion strengthening underlies asymmetric adherens junction contraction

Kate E. Cavanaugh,<sup>1,2</sup> Michael F. Staddon,<sup>3,4,5,8</sup> Theresa A. Chmiel,<sup>2,8</sup> Robert Harmon,<sup>2</sup> Srikanth Budnar,<sup>6,9</sup> Alpha S. Yap,<sup>6</sup> Shiladitya Banerjee,<sup>7</sup> and Margaret L. Gardel<sup>2,10,11,\*</sup>

<sup>1</sup>Committee on Development, Regeneration, and Stem Cell Biology, University of Chicago, Chicago, IL 60637, USA

<sup>2</sup>Institute for Biophysical Dynamics, James Franck Institute, Department of Physics, Pritzker School of Molecular Engineering, University of Chicago, Chicago, IL 60637, USA

<sup>3</sup>Center for Systems Biology Dresden, 01307 Dresden, Germany

<sup>4</sup>Max Planck Institute of Molecular Cell Biology and Genetics, 01307 Dresden, Germany

<sup>5</sup>Max Planck Institute for the Physics of Complex Systems, 01187 Dresden, Germany

<sup>6</sup>Division of Cell and Developmental Biology, Institute for Molecular Bioscience, The University of Queensland, St. Lucia, Brisbane, QLD 4072, Australia

<sup>7</sup>Department of Physics, Carnegie Mellon University, Pittsburgh, PA 15213, USA

<sup>8</sup>These authors contributed equally

<sup>9</sup>Present address: CSL Ltd, Bio21 Institute, Melbourne, VIC 3052, Australia

<sup>10</sup>Twitter: @squishywhole

<sup>11</sup>Lead contact

\*Correspondence: gardel@uchicago.edu

<https://doi.org/10.1016/j.cub.2022.03.024>

## SUMMARY

Tissue morphogenesis arises from the culmination of changes in cell-cell junction length. Mechanochemical signaling in the form of RhoA underlies these ratcheted contractions, which occur asymmetrically. The underlying mechanisms of asymmetry remain unknown. We use optogenetically controlled RhoA in model epithelia together with biophysical modeling to uncover the mechanism lending to asymmetric vertex motion. Using optogenetic and pharmacological approaches, we find that both local and global RhoA activation can drive asymmetric junction contraction in the absence of tissue-scale patterning. We find that standard vertex models with homogeneous junction properties are insufficient to recapitulate the observed junction dynamics. Furthermore, these experiments reveal a local coupling of RhoA activation with E-cadherin accumulation. This motivates a coupling of RhoA-mediated increases in tension and E-cadherin-mediated adhesion strengthening. We then demonstrate that incorporating this force-sensitive adhesion strengthening into a continuum model is successful in capturing the observed junction dynamics. Thus, we find that a force-dependent intercellular “clutch” at tricellular vertices stabilizes vertex motion under increasing tension and is sufficient to generate asymmetries in junction contraction.

## INTRODUCTION

Morphogenesis relies on the tight spatiotemporal control of cell-cell junction lengths.<sup>1</sup> Contractile forces, acting at adherens junctions, alter junction lengths as a cyclic ratchet.<sup>2–6</sup> Preceding these ratcheted contractions are pulses of active RhoA,<sup>5,7,8</sup> the strength and temporal pattern of which control junction tension to confer junction length.<sup>9,10</sup> Through effector activation, contractile actomyosin arrays assemble rapidly in response to intracellular biochemical signals and/or physical cues from neighboring cells.<sup>11</sup> As such, RhoA GTPase cycling is thought to give rise to spatiotemporal changes in junction length, which in turn drive tissue morphogenesis.<sup>12</sup> Although the molecular components of these mechanochemical systems are well characterized, the mechanisms by which RhoA regulates junctional tension and adhesion to control cell shape remain largely unknown.

A recent study has revealed the asymmetric nature of junction contraction that occurs during germband extension.<sup>13</sup> Here, one tricellular vertex is highly mobile and contracts toward a more immobile, stationary vertex. The net result of this asymmetric vertex motion is coordinated asymmetry in junction deformation whose collective contractions facilitate global tissue rearrangements.<sup>13,14</sup> A possible mechanism underlying this innate vertex asymmetry describes heterogeneous force production along the junction proper. Nonuniform force production may cause very local actomyosin to flow to specific regions of the junction for qualitatively different junctional responses. Bicellular edges, for example, act as independent contractile units apart from tricellular vertices.<sup>13,15</sup> Medioapical actomyosin that flows to the bicellular interfaces can also generate contractile forces sufficient to deform junctions<sup>5,8</sup> and to the tricellular vertices may restrict these contractions, thus stabilizing the junctional



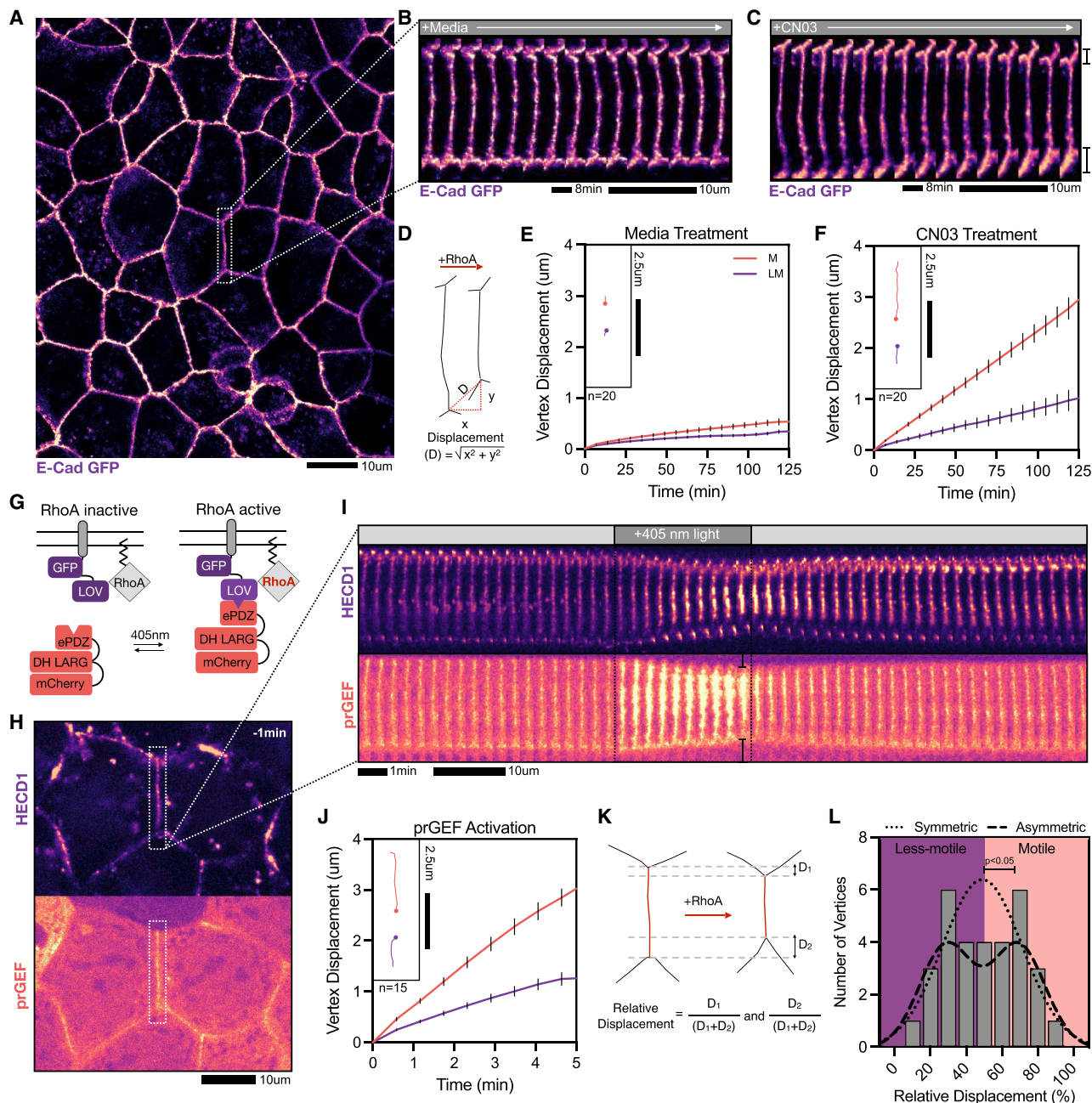


**Figure 1. RhoA activation drives asymmetric vertex motion in model tissue**

- (A) Representative image of a model epithelial tissue formed from confluent MDCK cells expressing E-cadherin GFP.
- (B) Zoomed-in images of the WT junction over the course of 2 h showing no junction length changes with the addition of media. See also [Figure S1](#) and [Video S1](#).
- (C) Representative images of time-lapse video over the course of 2 h showing asymmetric junction shortening with the addition of the CN03 compound. See also [Video S1](#).
- (D) Schematic of junction shortening and displacement measurement analysis.
- (E) Vertex displacement analysis for junctions under WT (media treatment) conditions showing little-to-no vertex motion. Inlay shows particle tracks for a representative vertex pair under WT conditions. Error bars indicate standard error. See also [Figure S1](#).
- (F) Vertex displacement analysis for junctions in CN03 treatment showing asymmetry in vertex displacements. Inlay shows trajectories for a representative vertex pair in CN03 treatment. Error bars indicate standard error. See also [Figure S1](#).
- (G) Schematic of the TULIP optogenetic system to drive local RhoA activation.
- (H) Zoomed-out image of a targeted junction at -1 min before optogenetic activation. Top image shows HECD1 junction labeling of E-cadherin and bottom image shows prGEF localization.
- (I) Time-lapse of the junction in H undergoing a 5-min optogenetic activation showing asymmetric junction contraction within the activation period and junction relaxation post-activation. See also [Figure S1](#) and [Video S2](#).

(legend continued on next page)

ratchet.<sup>13</sup> The coordination between these spatially distinct actomyosin flows may yield asymmetric junction shortening.<sup>13</sup> Thus, sub-cellular mechanics that underlies this asymmetry remains unclear.

Cells sense and respond to mechanical cues through force-sensitive feedbacks within the cytoskeleton. Apical E-cadherin-based adhesions mediate intercellular cell-cell adhesion. However, E-cadherin should be envisaged not as a static participant of cellular adherence but rather as a dynamic sensor of force that dictates cellular behavior. For example, force stimulates the RhoA pathway and myosin light chain phosphorylation, resulting in an overall increase in actin polymerization at adherens junctions.<sup>16</sup> Additionally, force-sensitive processes within adherens junctions allow adhesive components to strengthen under force.<sup>17</sup> Here, cadherin catch bonds are strengthened when adhesion complexes experience tensile force.<sup>18</sup> Together, these mechanisms cause clustering of E-cadherin molecules and actin to trigger adhesion complex growth.<sup>19</sup> In this way, these proteins subsequently generate a reinforcement response to anchor junctions against applied force.<sup>20</sup> However, it is still unclear if and how cells' force-sensitive coupling of actomyosin and adhesion complexes modulate junction length to coordinate morphogenetic movements at the cellular scale.

Here, we investigated the origins of asymmetric junction contraction by using optogenetic and pharmacologic modulation of RhoA activity. This system allowed for sub-cellular control of RhoA stimulation to investigate the origins of asymmetric contraction. We then used computational modeling to offer predictions on the mechanistic origin of this asymmetric contraction. Our experimental data indicated that differential regulation of vertex tension, as predicted by canonical models of epithelial tissues, was insufficient to account for such asymmetry. We then explored whether local coupling between RhoA-mediated contraction and vertex friction could account for the experimental results. We found that force-dependent adhesion strengthening at tricellular vertices acts to locally reinforce the vertex to restrict its movement. Thus, coupling between RhoA-mediated tension and adherens junction strengthening was sufficient to recapitulate experimental data. By modulating E-cadherin friction with pharmacological perturbations, we induced symmetry back into the system or abolished junction contraction entirely. Our modeling and experimental data therefore point to a unified model of asymmetry induced by both friction and local contraction that is mediated by a RhoA-dependent asymmetric recruitment of E-cadherin at tricellular vertices.

## RESULTS

### RhoA stimulates asymmetric junction contraction in a model epithelium

To examine how RhoA controls junction contractions, we formed a model tissue by plating a colorectal adenocarcinoma (Caco-2)

cell line at full confluence on collagen gels and CRISPR tagged for E-cadherin to facilitate the monitoring of junctional movements (Figure 1A).<sup>21</sup> We then measured junction length by finding the interfacial distance from one tricellular vertex to the other tricellular vertex. Under control conditions, there were negligible changes in junction length over the course of a 2-h period (Figures 1B and S1A; Video S1). Here, the junction length was stable and only fluctuated about 1% over the 2-h period (Figure 1B).

We then treated cells with a cell-permeable, pharmacological RhoA activator, CN03, to increase RhoA activity globally and acutely across the entire tissue. We began imaging upon the addition of CN03, at time ( $t$ ) = 0 min, and examined junction length changes resulting from RhoA increases until  $t$  = 125 min. About 30% of the junctions contracted, resulting in their shortening to about 80% of the initial length (Figures 1C and S1A; Video S1). We manually tracked each vertex and measured its displacement in space over time (Figure 1D). Under control conditions, we found that there was little-to-no vertex movement (Figures 1B and 1E). In contrast, in CN03-containing media, one vertex moved significantly more than the other vertex (Figures 1C and 1F). This asymmetric contraction is reminiscent of observations in developmental systems.<sup>13,14</sup>

To explore the mechanism of asymmetric contraction, we turned to an optogenetic approach. The logic behind this experiment was to have isolated junctions acutely experience heightened and targeted RhoA activation. For spatial and temporal control over RhoA activity, we used a Caco-2 cell line expressing the tunable light-controlled interacting protein (TULIP) optogenetic two-component system.<sup>9,10,22–24</sup> TULIP's two components include the (1) membrane-tethered photosensitive LOVpep anchor protein and the (2) photorecruitable guanine nucleotide exchange factor (prGEF) complex that houses the photorecruitable PDZ domain attached to the catalytic DH domain of the RhoA-specific GEF, LARG. Blue-light (405 nm) activation causes a conformational change in the LOVpep domain to expose a docking site for the engineered PDZ domain within the prGEF complex. This blue-light activation increases the binding affinity between the two components, thereby recruiting the prGEF to the membrane where it drives local RhoA activation (Figure 1G).<sup>9,10,22,24</sup> This system has high temporal resolution, as prGEF recruitment and dissociation occurs on the order of 30–60 s. prGEF recruitment was tightly confined to the targeted cell-cell junction, consistent with previously published work (Figure 1I).<sup>9</sup> This system is advantageous, because it restricts junctional contraction to the optogenetically activated junction, so that the frame of reference for vertex motion is the surrounding junctions and tissue. Overall, this system gave tight spatiotemporal control over the prGEF and thus RhoA in order to study how junctions contract upon increased RhoA activity.

To visualize the distortion of the bicellular junction during asymmetric contraction, we labeled E-cadherin using an

(J) Vertex displacement analysis for the junction within the 5-min optogenetic activation period. Displacement analysis shows asymmetric vertex displacement of the optogenetic Rho activation. Inlay shows particle tracks during the 5-min optogenetic activation period for a representative vertex pair. Error bars indicate standard error.

(K) Schematic documenting the percent movement analysis.

(L) A histogram of the percent motions of all vertices in response to optogenetic stimulation shows two peaks at 30% and 70%. A Hartigan's dip test ( $p = 0.049$ ) shows that the movement of the vertices is bimodal.

antibody labeling technique targeting its extracellular domain. We bathed the cells for at least an hour in E-cadherin primary antibody, HECD1, and its corresponding fluorescently labeled secondary antibody. Upon washing out the antibody, we found that this labeling produced a punctate pattern of E-cadherin that delineated the cell-cell junctions and vertices (Figures 1H and S1B). HECD1 targets the EC2 domain region of the E-cadherin ectodomain, rather than the EC1 domain that mediates trans-binding. In this way, cellular cohesion and intercellular E-cadherin binding via EC1 domains was preserved. Indeed, we found that under the conditions of our experiments, HECD1 did not affect junction contraction dynamics (Figures 1I and S1C–S1E; Video S2).<sup>9</sup> This light-stimulated contraction was surprisingly consistent across multiple junctions with different initial lengths and geometries.

We found that optogenetic recruitment of prGEF along the entire bicellular junction induced asymmetric contraction (Figures 1I and 1J; Video S2). To quantify the asymmetry, we measured the relative displacement of each vertex in a vertex pair, as defined by the distance moved of one vertex (e.g., D<sub>1</sub>) over the total distance moved by both vertices (D<sub>1</sub> + D<sub>2</sub>), to yield D<sub>1</sub>/(D<sub>1</sub> + D<sub>2</sub>) and D<sub>2</sub>/(D<sub>1</sub> + D<sub>2</sub>) (Figure 1K). We then plotted the probability density of the relative movement. This revealed an asymmetry in the histogram with peaks around 30% and 70%, further indicating an inherent asymmetry in the distribution of vertex motion (Figure 1L). This result was starkly contrasted against a symmetric contraction, where a single peak centered around 50% would be expected. Interestingly, this asymmetric vertex displacement occurred despite uniform prGEF recruitment along the bicellular junction, discarding the possibility that heterogenous GEF recruitment is required for asymmetric junction contraction (Figures S1F and S1G). The asymmetric contraction of junctions was also surprisingly robust to changes in focal adhesion signaling (Figures S1H–S1O).

#### Asymmetric contraction can be driven by heterogeneity in active RhoA

Junctions could either contract uniformly along their length or the extent of contraction could vary as a function of position. To explore these possibilities, we used the variable intensity of HECD1 labeling to examine local variations in deformations along the junction. A line scan along the junction, taken over time, created a kymograph for which to analyze fiduciary flows before, during, and after light-stimulated junction contraction (Figure 2A).

Using these kymographs, we then measured the displacement of different regions along the junction over time (Figure 2A). We identified the location of zero displacement to identify the contraction center. To compare junctions of varying lengths, we normalized both displacement and position along the junction by the junction length. For consistency, we identified the less mobile vertex position as “0” and the more mobile vertex position as “1.” For a symmetric contraction, we would expect to see the center of contraction at the midpoint of the junction, or 0.5, and a displacement proportional to distance from the contraction center. Instead, we found that the displacement is nonlinear, suggesting that contraction is heterogenous along the bicellular junction (Figure 2B). Furthermore, we found the contraction center to be skewed toward the less-motile (LM)

vertex (Figures 2A and 2C). Analyzing multiple kymographs revealed that the mean center of junction contraction was consistently closer to the LM vertex with a mean of 0.32 (Figure 2C). By contrast, values of normalized center of contraction over 0.5 would be achieved in scenarios in which the center of contraction is proximal to the motile vertex.

It is plausible that that RhoA activity is not uniform along the junctions, giving rise to heterogeneous stress along the junction. To explore this, we used the RhoA biosensor (AHPH) containing the GTP-RhoA binding C-terminal portion of Anillin.<sup>25,26</sup> We transfected the E-cadherin-expressing cells with the AHPH and then visualized RhoA activity during a CN03 wash-in experiment. We observed discrete sub-junctional region of heightened active RhoA, which we termed flares (Figures 2D and 2E; Video S3). These flares were absent from junctions without CN03 treatment (Figures S2A–S2F). We measured the intensity of active RhoA along the junction and found that the peak, the central flare location, was skewed toward the LM vertex (Figures 2D and 2E; Video S3). Fitting a Gaussian curve to these data, we labeled the peak of this Gaussian as the location of the “peak” RhoA region (Figure 2E). By analyzing fourteen kymographs, we found that the mean RhoA flare position was skewed toward the LM vertex, with an average position of 0.35 (Figure 2F).

The above data indicated that the location of RhoA flares were critical in determining asymmetric contraction, with reduced mobility of the vertex proximal to active RhoA. To test this hypothesis, we exploited the optogenetic approach to systematically activate only a portion of the junction. When the lower half of the junction was activated, the junction contracted to about 85% of its original length, similar to the extent for full junction activation. The vertex proximal to the region of activation (ROA) was significantly less mobile than the distal vertex (Figures 2G and 2H; Video S4). Kymograph analysis in the HECD1 channel revealed that the center of contraction for the half-junction activation was at the relative position of 0.2 (Figure 2I). Altogether these data indicate that asymmetry in active RhoA dictates the bias in vertex motion.

#### Mechanosensitive E-cadherin induces vertex friction at LM vertices

RhoA acts at cell-cell interfaces to regulate cell morphology through its effect on actomyosin tension and adhesion strength.<sup>9,27</sup> To explore the possibility that changes in adhesion strength underlie vertex immobility, we analyzed E-cadherin localization, as visualized by HECD1 fluorescence, at tricellular vertices during whole junction optogenetic stimulation. We observed HECD1 fluorescence in punctae along the junction and at both vertices. We monitored the HECD1 fluorescence at both vertices during an activation experiment. At the more motile (M) vertex, we found that the HECD1 intensity did not vary significantly during the experiment (Figure 3A [red arrow]). By contrast, at the LM vertex, we found that there was a marked increase in HECD1 immediately after activation which diminished after exogenous stimulation was removed (Figures 3A and 3B; Video S5). This trend was consistent across numerous junctions and paired vertices (Figure 3C). To further explore the contribution of E-cadherin levels to vertex asymmetry, we analyzed the relative HECD1 fluorescence intensities between the M and LM vertices. We found that before optogenetic activation, at T<sub>0</sub>,

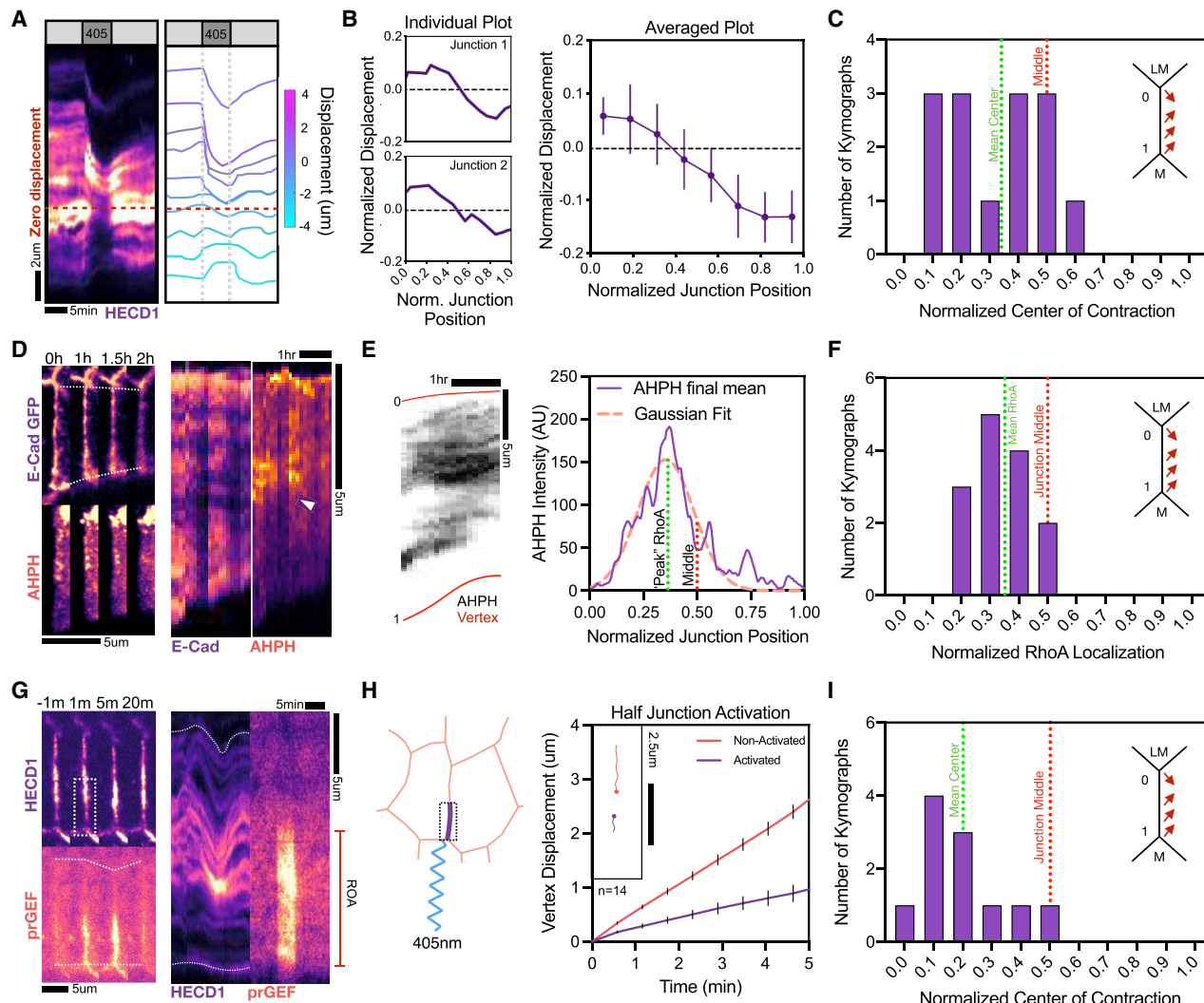


**Figure 2. Asymmetric distribution of active RhoA drives contraction asymmetry**

(A) (Left) Representative kymograph of an optogenetically activated junction labeled with HECD1 showing asymmetry junction contraction and relaxation. (Right) Fiducial marks seen in the kymograph to the left are color coded according to the amount of displacement within the optogenetic activation period. The location of zero displacement of the fiducial marks is marked with a dashed red line.

(B) (Left) Analysis of the displacement of each fiducial mark's flows as a function of the distance from the contraction center for two individual junctions showing nonlinear displacement from one end of the junction to the other, indicating a nonuniform contraction of each junction. (Right) Averaged plot showing the nonlinearity of fiducial displacement as a function of the normalized junction position. Error bars show standard deviation.

(C) Inlay shows diagram of the less-motile (LM) vertex being labeled as 0 and the motile (M) vertex being labeled as 1. Red arrows represent the extent of the vertex motion along the junction during contraction. Analysis of the localization of zero displacement (as seen in A) of the fiduciary marks indicates the center of the junction as being skewed toward the less-motile vertex.

(D) (Left) Representative image E-cadherin-GFP and RhoA biosensor, AHPH in a junction subjected to CN03 treatment. Junction shows asymmetric contraction with a RhoA flare along the junction. (Right) Kymographs show asymmetric junction contraction and a RhoA flare that is biased toward the less-motile vertex. See also Figure S2 and Video S3.

(E) Analysis of the junctional AHPH intensity plots averaged over the last 5 frames of the kymograph (left) fitted to a Gaussian curve. Green dotted line indicates the peak of the Gaussian fit, indicating the centralized location of the RhoA biosensor.

(F) Pooled analysis of the peak of the RhoA biosensor, as calculated in (E), showing mean junctional RhoA localization as being skewed toward the less-motile vertex.

(G) Representative image and kymograph of a junction undergoing half-junction activation at the bottom junctional region. See also Video S4.

(H) Vertex displacement analysis of bottom-junction activation showing contractile asymmetry between two vertices. Inlay shows individual vertex tracks for two vertices of the same junction. Error bars indicate standard error.

(I) Normalized center of contraction analysis for bottom-junction activation showing the center of contraction is skewed toward the region of activation.

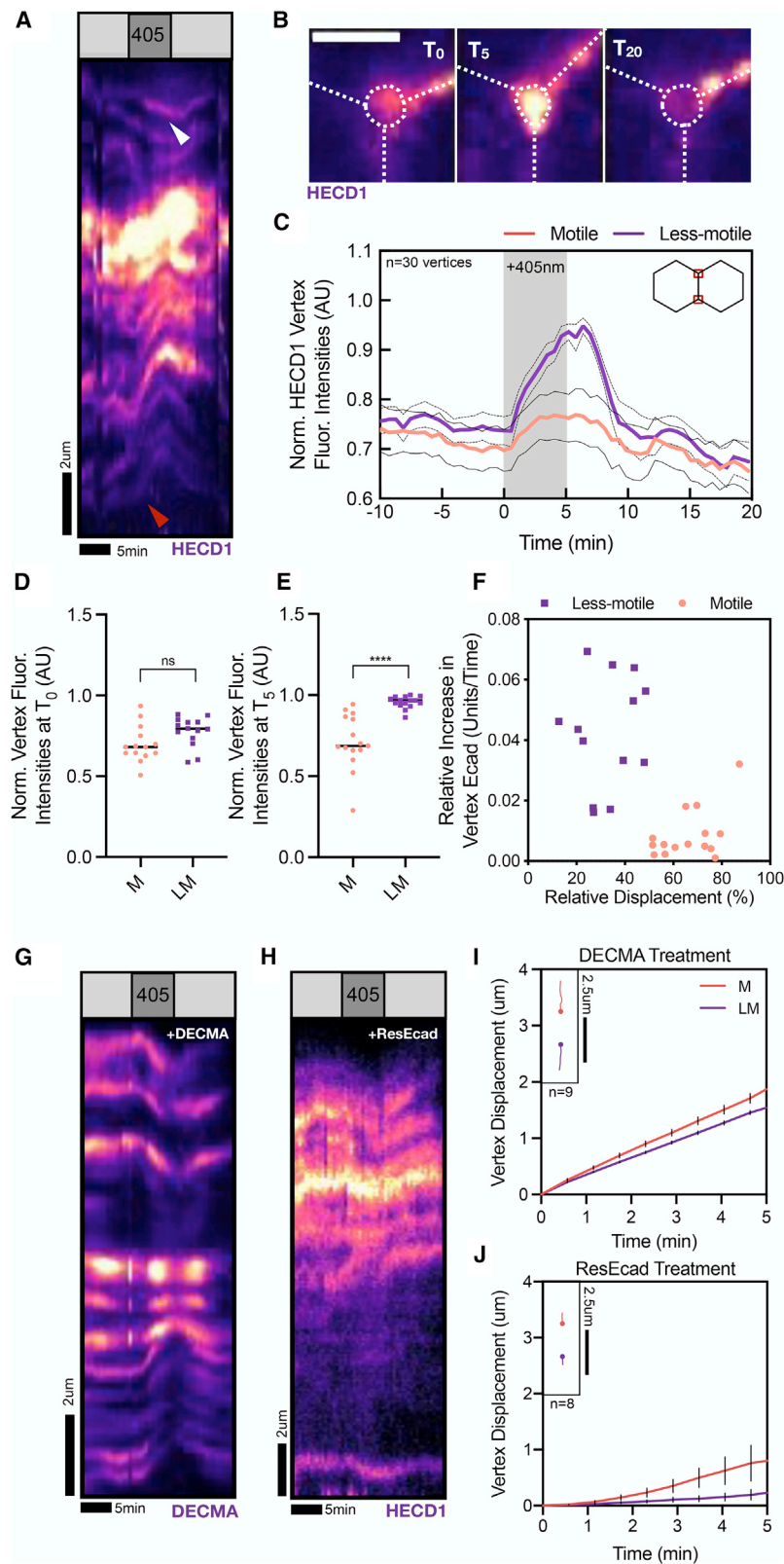


**Figure 3. E-cadherin accumulates at less-motile vertex and perturbations to E-cad alter contraction dynamics**

(A) Representative kymograph of optogenetic activation showing increases in E-cadherin pooling at the less-motile vertex (white arrow) versus the motile vertex (red arrow). (B) Representative image of a less-motile tricellular contact showing E-cadherin pooling at the vertex after 5 min of optogenetic activation. Scale bars, 2.5 μm. See also Video S5.

(C) Quantification of vertex fluorescence intensities of motile and less-motile vertices. Less-motile vertices show increases in E-cadherin pooling and subsequent vertex fluorescence compared with motile vertices.

(D) Quantification of the normalized HECD1 fluorescence vertex intensities before optogenetic activation at T<sub>0</sub> for motile and less-motile vertex shows no significant difference.

(E) Quantification of the normalized HECD1 fluorescence vertex intensities after optogenetic activation at T<sub>5</sub> for motile and less-motile vertex shows a significant, heightened level of E-cadherin at less-motile vertices. \*\*\*p < 0.0001 as calculated by the Student's t test.

(F) Relative increases of the vertex HECD1 (E-cad) plotted against the relative displacement of that vertex shows highly motile vertices with less HECD1 changes and less-motile vertices showing more HECD1 level changes.

(G) Representative kymograph of junction treated with the E-cadherin blocking antibody, DECMA. See also Video S6.

(H) Representative kymograph of cells treated with ResEcad. See also Figure S3 and Video S6.

(I) Vertex displacement analysis of DECMA-treated junctions showing symmetric contraction. Inlay shows particle tracks of a representative vertex pair during optogenetic activation. Error bars indicate standard error.

(J) Vertex displacement analysis of ResEcad-treated junctions showing a severe reduction in the contraction. Inlay shows particle tracks of a representative vertex pair during optogenetic activation. Error bars indicate standard error.

we found no significant difference in normalized vertex HECD1 fluorescence intensities (Figure 3D). After 5 min of optogenetic activation, at T<sub>5</sub>, we found a significant increase in HECD1 fluorescence intensities at the LM vertex compared with those at the M vertex (Figure 3E). We then plotted the relative increase in vertex HECD1 as a function of the relative displacement of each vertex and saw a clear trend suggesting that the higher the relative increase in E-cadherin, the less the vertex would move in space, thus promoting vertex asymmetry (Figure 3F). Together, these data indicate that changes in tricellular junction adhesion strength may contribute to the observed asymmetry.

To explore whether E-cadherin-mediated adhesion acts to impede contraction via its contribution as a source of frictional drag, we next sought to modulate E-cadherin interactions. First, we used a function blocking antibody, DECMA, and its conjugated secondary antibody to visualize junctional dynamics. DECMA binds specifically to EC1 domains on E-cadherin, abolishing any trans-interactions between E-cadherin molecules, thereby reducing E-cadherin binding. Upon addition of DECMA, we found a similar labeling pattern of E-cadherin that coated the junction (Figure 3G). Optogenetic activation induced similar junctional contractions compared with WT conditions, but the contraction was more symmetric (Figures 3G–3I; Video S6). To increase junctional friction, we next sought to increase the levels of E-cadherin through the cell-permeable, pharmacological isoxazolocarboxamide compound, ResEcad<sup>28</sup> (Figure S3A). This compound has been shown to induce a dose-dependent increase in E-cadherin levels in adenocarcinoma cells, thereby modulating junctional friction levels. We found that ResEcad treatment severely suppressed optogenetically induced junction contraction (Figures 3H, 3J, S3B, and S3C; Video S6). These data indicate that modulating E-cadherin levels and interactions, inducing either low or high adhesion strength, can dramatically influence both the magnitude and asymmetric nature of vertex motions.

### Local RhoA drives E-cadherin accumulation

The above data hint at active RhoA driving E-cadherin recruitment to modify adhesion strength along the bicellular or tricellular junction, an idea that has been explored recently.<sup>29,30</sup> To explore this, we used our optogenetic approach to selectively recruit prGEF to the tricellular junction or a small portion of the bicellular junction. Interestingly, tricellular vertex prGEF recruitment was insufficient to induce junction contraction, with the vertices exhibiting little-to-no vertex displacement compared with WT full-length activation (Figures 4A and 4B; Video S7). However, tricellular vertex activation did induce a 30% increase in E-cadherin intensity (Figures 4A and 4C). These data indicated that RhoA activation locally recruits E-cadherin, even in the absence of visible junction contraction.

We next activated a small portion of the bicellular junction (Figure 4D; Video S7). Activation at the center third of the junction created a contraction whose extent was similar to that of WT full-length activation. As the center was being activated, there was a noticeable concentration of E-cadherin puncta to the ROA (Figure 4D). Displacement analysis for the center activation indicated that the contraction was more symmetric, with both vertices moving considerably and relatively evenly upon prGEF recruitment (Figure 4E). Moreover, analysis of the HECD1 fiducial marks revealed that the center of contraction

was symmetric, with a mean center of contraction of 0.47 (Figure 4H).

We observed E-cadherin accumulation with this stimulation geometry, which also provided a means to explore its possible mechanisms. E-cadherin punctae coalescence upon junctional prGEF recruitment within the activation period (Figure 4G). Here, prGEF recruitment preceded this concentration of E-cadherin, as smaller punctae of E-cadherin coalesced to a concentrated point upon blue-light activation (Figure 4G [white arrows]; Video S7). We then measured the fluorescence intensities of the HECD1 at the ROA and the non-activated flanking regions (Figure 4H). This analysis revealed heightened accumulation of HECD1 at the ROA compared with the distal portion, where the overall intensity change was negligible. There was no depletion of HECD1 fluorescence intensities within the flanking regions, indicating minimal lateral motion of punctae from the flanking to activated region. Rather, these data led us to suspect that E-cadherin accumulation occurs from diffuse membrane-associated E-cadherin, including from those regions outside the focal plane and/or along the basolateral interface. Furthermore, the coalescences suggest that the punctae are relatively stable and accumulate intensity from diffusing E-cadherin. This is not dissimilar to the increase in intensity of focal adhesion proteins within plaques during their assembly.<sup>31</sup>

Together, these data hint that junctional RhoA activity serves both to generate stresses required for contraction, as well as modify cell-cell adhesion through E-cadherin recruitment. Thus, we surmise that their coordination drives the nature of junction contraction, which we explore with mathematical modeling.

### Mechanical model of asymmetric junction contraction

To quantitatively explain the biomechanical origins of the observed asymmetric contraction, we developed a continuum mechanical model for the junction dynamics arising from the balance of tensional forces of the primary junction with the two neighboring shoulder junctions and a frictional drag acting at the vertices to resist their motion (Figures 5A and 5B). We modeled the junction as a linear elastic continuum with compressional elastic modulus  $E$ , tension  $A$ , and dissipating stresses with a friction coefficient  $\mu$ . The shoulder junctions provide an elastic spring-like resistance to motion with stiffness  $k$ . We surmise that the regions flanking those of heightened tension are the primary source of friction and are dominated by the shoulder junctions and/or the bicellular interface. Building upon molecular clutch models regulating cell adhesion,<sup>30,32</sup> we surmise that friction arises from the relative motion between the E-cadherin-bound membrane and the actin cortex, mediated by turnover of linkers, such as the ezrin-radixin-moesin (ERM) proteins,  $\alpha$ - and  $\beta$ -catenins, as well as from differential motion of the contracting junction with the flanking shoulder junctions (Figure 5A).

Our continuum modeling approach for the intercellular junction stood in contrast to the existing vertex models of epithelial tissues,<sup>33–35</sup> where the epithelia are modeled as networks of edges under uniform and constant tension,<sup>36</sup> with the vertex positions determined by force balance from the neighboring junctions. By modeling the junction as an elastic continuum, we

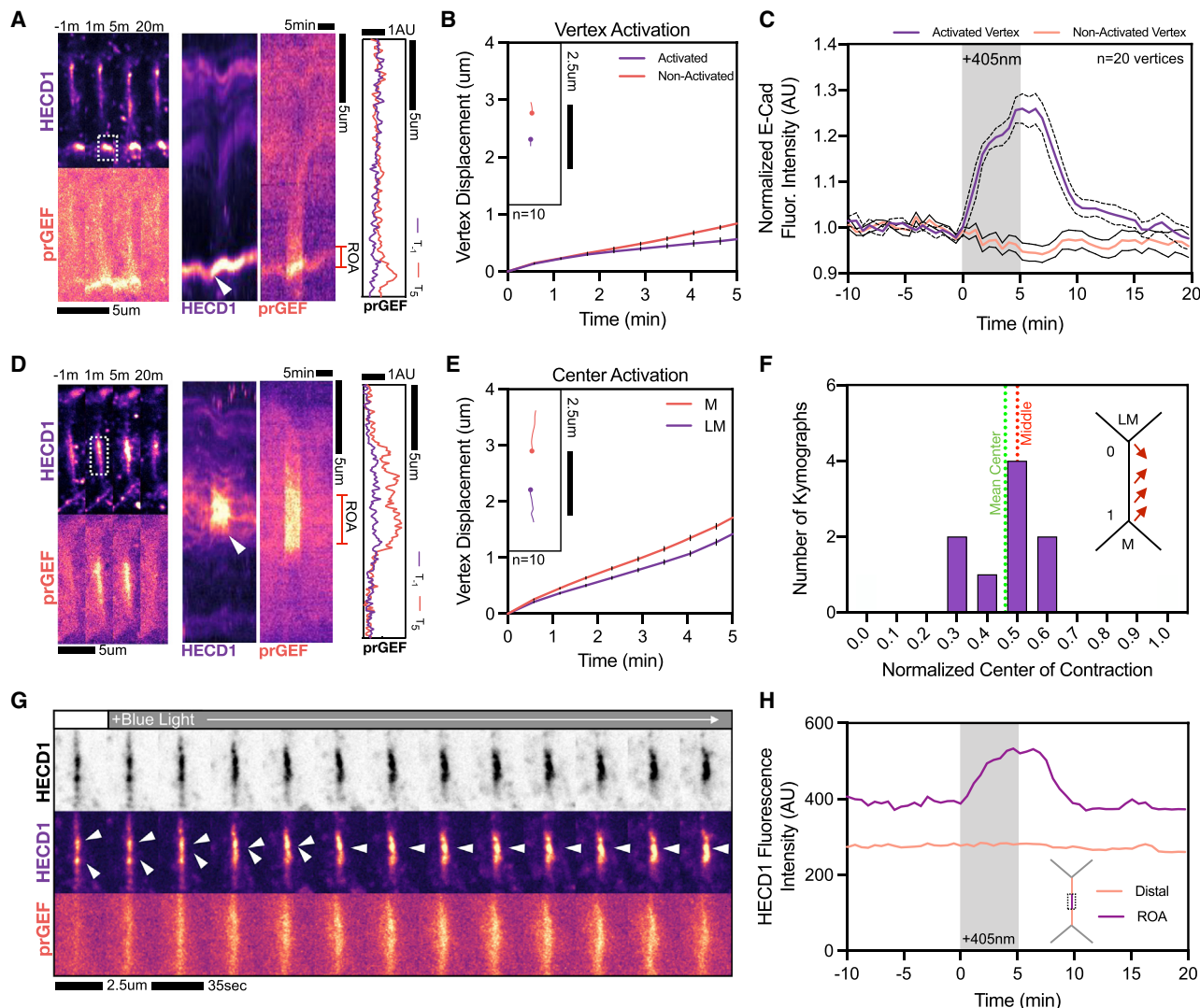


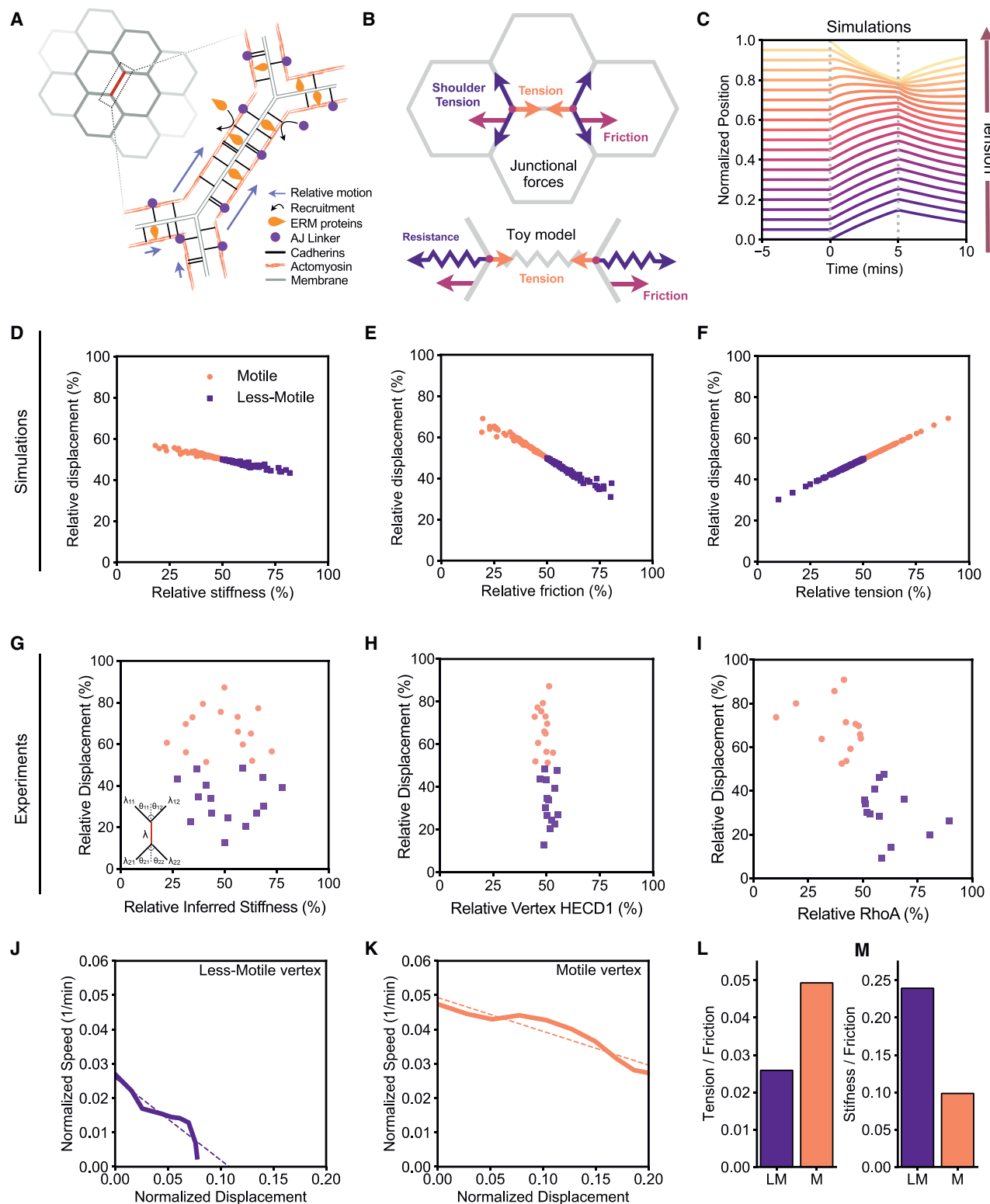
**Figure 4. RhoA activation drives local E-cadherin accumulation**

- (A) Representative image and kymograph of a junction undergoing only vertex activation at the tricellular contact. See also [Video S7](#).
- (B) Vertex displacement analysis of vertex activation showing little-to-no vertex motion within the optogenetic activation period. Inlay shows individual vertex tracks for two vertices of the same junction. Error bars indicate standard error.
- (C) Normalized HECD1 (E-cadherin) fluorescence intensities for vertices during vertex activation between the activated and non-activated vertices. Activated vertices show increases in E-cadherin fluorescence intensities.
- (D) Representative image and kymograph of a junction undergoing center-junction activation. See also [Video S7](#).
- (E) Vertex displacement analysis of center-junction activation showing contractile symmetry is restored. Inlay shows individual vertex tracks for two vertices of the same junction. Error bars indicate standard error.
- (F) Normalized center of contraction analysis for center-junction activation showing the center of contraction is in the middle of the junction, consistent with where RhoA is activated.
- (G) Representative images of HECD1 and prGEF before and during optogenetic activation, showing displacement E-cadherin puncta upon activation (white arrows). See also [Video S7](#).
- (H) Quantification of average fluorescence intensities of HECD1 of data in (G) both within the region of activation (ROA) and the two flanking regions proximal to the ROA.

allowed for the junction tension and friction forces to vary along the length of the junction, such that the displacement along the junction would be tracked during a contraction event ([Figure 5C](#)). Mechanical force balance at a point along the junction was written as

$$\mu \frac{\partial u}{\partial t} = E \frac{\partial^2 u}{\partial x^2} + \frac{\partial J}{\partial x} \quad (\text{Equation 1})$$

where  $u(x, t)$  was the displacement along the junction at time  $t$ , and  $x$  was the position along the junction. The shoulder junctions

**Figure 5. Mechanical forces regulating vertex motion asymmetry**

(A) Schematic showing a single junction's architecture at the bicellular interface, with speculation on molecular-scale interactions built from the existing literature.

(B) Toy model schematic, illustrating the forces that control junction contraction dynamics. Shoulder junctions are modeled through a spring-like tensions and friction that resist the extent and rate of deformation. Junction is modeled as an elastic continuum, where tension and friction may vary along the junction and at the vertices.

(legend continued on next page)

were modeled as providing a spring-like resistance to motion, with an effective stiffness  $k$  that depended both on the tension and the geometry of the shoulder junctions (see “[computational model](#)” section). For simplicity, we normalize distance by the length of the junction, such that  $x = 0$  and  $x = 1$  are the ends of the junction, and normalize stresses by the Young’s modulus of the junction, only keeping the units of time. Force balance at the tricellular vertices was given by

$$\mu \frac{\partial u}{\partial t} = E \frac{\partial u}{\partial x} + \Lambda - k_{LM}u \quad (\text{Equation 2})$$

at  $x = 0$  and

$$\mu \frac{\partial u}{\partial t} = -E \frac{\partial u}{\partial x} - \Lambda - k_M u \quad (\text{Equation 3})$$

at  $x = 1$ , with  $k_{LM}$  and  $k_M$  being the stiffnesses of the two shoulder junctions corresponding to the LM and the M vertices, respectively. We estimate the model parameters by analyzing the motion of vertices measured in experiments ([Figures S4G–S4I](#)). When plotting vertex speed against displacement, we observe an approximate linear trend ([Figure S4I](#)). Assuming a simple linear spring model for the effective elastic response at each vertex,  $\dot{u}_i = (\Lambda_i - (k_i + E)u_i)/\mu_i$ , where  $\Lambda_i$  is the tension acting on the vertex  $i$  ( $i = LM, M$ ),  $\mu_i$  is the friction, and  $k_i$  is the shoulder stiffness, we estimate the tension to friction ratio  $\Lambda_i/\mu_i$  from the intercept, and stiffness to friction ratio  $(k_i + E)/\mu_i$  from the slope of the speed-displacement curve ([STAR Methods](#)).

To simulate RhoA-induced contraction, we applied a uniform contractile stress for a duration of 5 min to a junction initially at rest and recorded the resulting displacements of the two vertices ([Figure 5C](#)). These displacements were obtained by solving [Equation 1](#) subject to the boundary conditions given by [Equations 2](#) and [3](#). We then used the model to test three different mechanisms for asymmetric vertex motion and heterogeneous mechanical response arising from (1) differential elastic resistance at the shoulder junctions, (2) differential friction, and (3) asymmetric tension along the junction.

We first tested how the asymmetry in vertex motion was regulated by differential elastic resistance from the shoulder junctions using our continuum mechanical model. For each vertex, we sampled the shoulder junction stiffness  $k_i$  from a normal distribution with mean  $k_0$  and standard deviation  $k_0/3$ . For each vertex, we then compared the percentage of total vertex displacement (relative displacement),  $u_i/(u_{LM} + u_M)$ , against the percentage

of total shoulder stiffness (relative stiffness),  $k_i/(k_{LM} + k_M)$ . Expectedly, we found that vertex displacement depended linearly on shoulder stiffness, with relative displacement decreasing with increasing relative stiffness ([Figure 5D](#)).

To test the model predictions using our experimental data, we estimated the elastic resistance at shoulder junctions by computing the tensions along shoulder junctions and change in their geometries during a contraction event, as measured by calculating junction length and the interior angles normal to the activated junction ([STAR Methods](#)). From the angles between the activated junction and its neighbors, we calculated the relative tensions on each junction by balancing forces both along the junction and perpendicular to it. From these tensions, we then calculated the differential change in force due to a change in vertex position, which defines the effective stiffness of the shoulder junctions ([STAR Methods](#)). However, when we quantified the relative stiffness using data from our optogenetic experiments, we found no correlation with relative vertex displacement ([Figure 5G](#)), indicating that asymmetric elastic resistance at the vertices does not play a role in predicting asymmetric vertex motion upon contraction.

An alternative mechanism for asymmetric vertex motion could arise from heterogeneous adhesive properties at the tricellular vertices or even along the junction proper that may alter the frictional drag. Indeed, our experimental data showed that there is a marked increase in E-cadherin levels at the LM vertex compared with the motile one during an optogenetic activation ([Figure 3A](#)). We therefore sought to test if different frictional forces at the vertices could capture the asymmetric vertex motion. At each vertex, friction was set to a random value sampled from a normal distribution with mean  $\mu_0$  and standard deviation  $\mu_0/3$ , and values were linearly interpolated along the junction. We found a linear dependence of relative displacement on relative friction  $\mu_i/(\mu_{LM} + \mu_M)$ , with  $\mu_{LM}$  and  $\mu_M$  being the friction coefficient at the less-motile and the motile vertices, such that increased friction resulted in reduced motion ([Figure 5E](#)). As an estimate of the friction in experimental measurements, we measured the relative percentage of HECD1 at each vertex compared with the total amount of HECD1 within each vertex pair. To our surprise, we did not find any correlation between vertex motion and initial cadherin-mediated friction ([Figure 5H](#)). Instead, we found that HECD1 intensities were relatively even between each vertex before optogenetic activation.

Finally, we considered the effects of varying tension along the junction induced by RhoA-mediated contractility. We varied tension along the junction by setting the tension at each vertex to be

- (C) Kymograph of simulation junction during contraction. Lines show the motion of points along the junction with brighter colors showing higher tension, with  $\Lambda(0) = 1$ ,  $\Lambda(1) = 2$ .
  - (D) Simulation results of the relative displacement of the two vertices as a function of their relative stiffness.
  - (E) Simulation results of the relative displacement of two vertices as a function of their relative friction.
  - (F) Simulations results of the relative displacement of two vertices as a function of their relative tension.
  - (G) Experimental data plotting relative motion as a function of relative stiffness.
  - (H) Experimental data of relative displacement as a function of the HECD1 intensity ratio at T-10 before optogenetic activation.
  - (I) Experimental data plotting relative displacement as a function of the RhoA percentage at each vertex.
  - (J and K) Average normalized speed against normalized position from experiments for (J) the less-motile vertex, and (K) the motile vertex. Dashed line indicates a linear fit. See also [Figure S4](#).
  - (L and M) (L) Tension over friction, equal to the intercept of the fit, and (M) stiffness over friction, equal to the gradient of the fit, for the less-motile and motile vertices.
- See also [Figure S4](#).

a random value sampled from a normal distribution with mean  $A_0$  and standard deviation  $A_0/3$  and linearly interpolated tension along the junction. We found that vertices under higher tension (more contractility) underwent larger displacements (Figure 5F). To measure relative junction tension, we returned to our CN03 wash-in experiments to measure RhoA intensities. We split the junction into two halves and measured the relative intensity of AHPH at each junctional portion compared with the total amount of AHPH along the junction proper. Plotting relative displacement as a function of this percentage of RhoA intensity, we found a correlation between less-motile vertices and the relative amount of junctional RhoA present (Figure 5I). Here, data suggested that the closer the RhoA was to a vertex, the less it moved, consistent with our data in Figure 2G. This was starkly contrasted to highly motile vertices, which were distal to RhoA regions and experienced little RhoA-mediated tension. Together, these data suggest that asymmetries in friction, tension, and stiffness parameters alone were insufficient to explain asymmetries in vertex movement during junction contractions.

#### RhoA recruitment of E-cadherin reduces vertex motion

Our experimental data demonstrated that vertices with higher recruitment of RhoA moved less (Figure 2). In contrast, simulations predicted that tension increased proximal vertex displacements (Figure 5F). At the same time, less mobile vertices also showed a marked increase in E-cadherin levels during an optogenetic activation (Figures 3A–3C). This suggests a likely coupling between force and adhesion strength. To explore how these change over time, we plotted the normalized vertex speed as a function of its normalized displacement (Figures 5J, 5K, and S4A–S4F). We observe that the initial velocity of the less-motile vertex is smaller than the motile vertex (Figures 5J and 5K [y-intercept]). Moreover, the less-motile vertex slows down more rapidly over time (Figures 5J and 5K [slopes of curves]). By assuming a simple linear spring model for vertex displacements,  $\dot{u}_i = (A_i - (k_i + E)u_i)/\mu_i$ , we can make estimates of the tension and stiffness relative to the friction (STAR Methods) and find that the ratio of the tension to friction is lower in the LM vertex than in the M vertex (Figure 5L). However, the LM vertex also has higher levels of RhoA, which suggests higher levels of tension. Thus, the overall friction in the less-motile vertex must be overall higher than that of the motile one. Furthermore, since the experimental data showed a higher ratio of stiffness to friction in the less-motile vertices (Figure 5M), the local effective stiffness of these is much higher than that of the motile vertices.

These experimental data motivate introducing a coupling into our model, such that the friction is tension-dependent (Figure 6A). This is conceptually similar to previously described tension-dependent strengthening of focal adhesions.<sup>32</sup> With a high coupling between tension and friction, an increase in tension would increase friction to such an extent that the vertex would move slower. Thus, we allowed tension-dependent friction and stiffness by tension along the junction in our continuum model. Again, we varied tension along the junction by setting the tension at each vertex to be a random value sampled from the normal distribution with mean  $A_0$  and standard deviation  $A_0/3$ , and linearly interpolated tension along the junction. Using a low-force catch bond model, the friction coefficient was given by  $\mu(A) =$

$\mu_M(\mu_{LM}/\mu_M)^{1-1}$ , where  $\mu_M$  and  $\mu_{LM}$  are the estimated mean friction coefficients at the motile and non-motile vertices, respectively. Similarly, the shoulder stiffness increases with tension  $k(A) = k_M(k_{LM}/k_M)^{1-1}$ , where  $k_M$  and  $k_{LM}$  are the estimated mean stiffnesses at the motile and non-motile vertices, respectively (Figure 6A).

Adding this coupling into the model is sufficient to quantitatively reproduce the experimental data heterogeneous junction contraction (Figures 6B and 6C), the asymmetric vertex displacement (Figure 6D) and the vertices speeds over time (Figures 6E and S4) and the inverse correlation between relative displacement and tension (Figure 6F compared with Figure 5I). Thus, together these support the notion that force-dependent recruitment of E-cadherin results in increased adhesion strength (e.g., friction) and stiffness at the vertex. Indeed, ours and others' data point to a common coupling mechanism between junctional RhoA and E-cadherin, modulation of which alters the frictional landscape of tricellular vertices.<sup>29,30,37</sup>

We further test this model by applying partial activations of contractility in our model (Figure S5). By increasing tension to just half of the junction near one of the vertices, we find that the activated vertex moves less than the non-activated one, in agreement with experiments, due to the increased friction and stiffness from the shoulders (Figures S5A–S5C). In contrast, if we have no force-dependent adhesion strengthening, we find more motion at the activated junction (Figures S5D–S5F). When we activate just the center third, we see equal motion at the two vertices (Figures S5G–S5I). These simulations, coupled with experimental data, indicated that the E-cadherin recruitment at tricellular vertices likely increased the local friction coefficient and shoulder stiffness to limit junction contraction in a RhoA-dependent manner.

#### DISCUSSION

We present here a new model for vertex mechanoresponse that successfully recapitulates asymmetric junction contraction via a coupling between local tension and E-cadherin-mediated adhesion strengthening (Figure 6G). We find that RhoA-dependent contraction induces a heterogeneous contraction of the bicellular junction, with the center of contraction and RhoA localization skewed toward the less-motile vertex. In order to quantitatively model these data, we find that asymmetries in junctional stiffness, friction, and tension parameters alone cannot successfully recapitulate experimental data. Instead, we suggest a coupling of friction with tension such that local RhoA induces both tension and E-cadherin recruitment to increase adhesion strength (and associated friction). Described previously for focal adhesions, this coupling is a natural means to reduce vertex mobility as force increases.<sup>32</sup> Incorporating this coupling into our quantitative model, we were able to successfully recapitulate the observed dynamics of RhoA-induced junction contraction. Needless to say, the complex feedbacks underlying cell junction dynamics make it difficult to constrain such models and other plausible physical models, including variation in junction elasticity and viscosity, may likely exist.

Our study supports a “clutch” model for tricellular contact engagement during junction contraction. In the absence of RhoA activity, or at distal regions with less RhoA, little

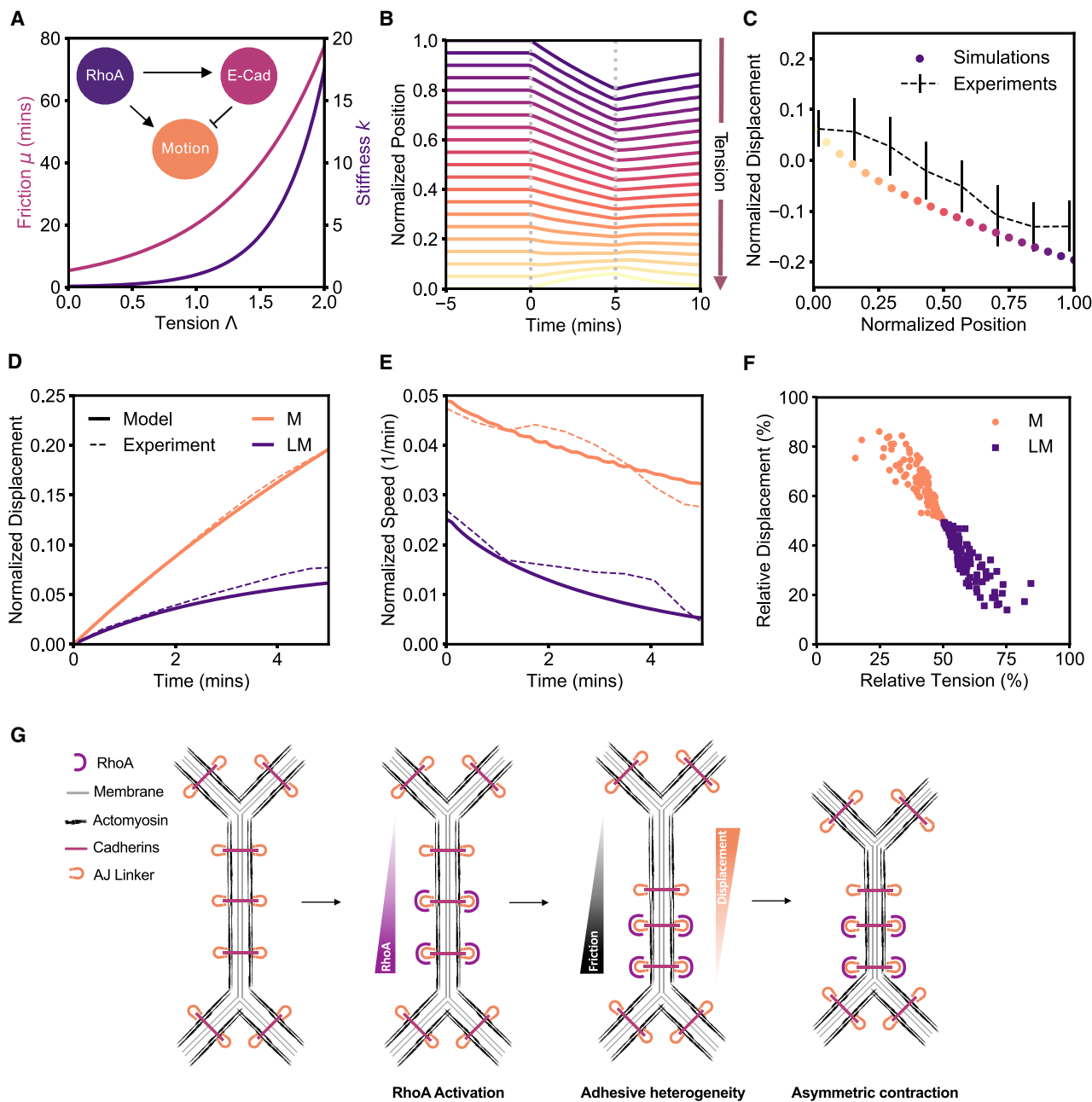


**Figure 6. Force-dependent adhesion strengthening is sufficient to recapitulate junction dynamics**

- (A) Illustrative coupling of adhesion strength (friction) to tension for strong (pink) and weaker (purple) coupling values. Inset: Rho-dependent increases in E-cadherin adhesion will counteract its effects on local motion. See also [Figure S5](#).
- (B) Simulated kymograph of junction contraction that includes this coupling. Lines show the motion of points along the junction, with brighter colors showing higher tension, using the best fit parameters. See also [Figure S5](#).
- (C) Simulated (dots) and experimental (lines) relative displacement against relative position. Error bars show standard deviation. See also [Figure S5](#).
- (D and E) (D) Vertex displacement and (E) vertex speed over time using best fit parameters in the model (solid lines), and in experiments (dashed lines). See also [Figure S5](#).
- (F) Normalized displacement against relative tension for the model (solid line), using randomly distributed tensions.
- (G) Schematic of illustrating how RhoA-Ecad coupling underlying force-dependent adhesion facilitates asymmetric contraction. The junction (actin, black; membrane, gray) with cadherin-based adhesions (purple rods) and respective adhesive linkers (orange barbells) shows homeostasis before RhoA activation (Purple barbells). Upon RhoA recruitment, there is a gradient of RhoA that forms an asymmetry along the junction that increases locally the friction and lowers the motility of the proximal vertex. This friction gradient induces asymmetric contraction.

E-cadherin is recruited to the vertices. When RhoA-mediated tension is applied to the junction, proximal tricellular adhesions undergo a rapid accumulation of E-cadherin to strengthen adhesion and restrict motion in a process similar to that previously in focal adhesions.<sup>32</sup> We envision a similar mechanism operating at tricellular vertices such that mechanosensitive reinforcement of tricellular contacts engages the clutch to strengthen adhesions under load. This adhesion reinforcement restricts vertex motions asymmetrically, as RhoA-mediated tension is stochastically skewed toward one vertex.

These data beg the question as to how RhoA is stochastically placed along the junction. We believe the junction is split into discrete domains that are primed for RhoA activation. These primed regions could be borne out of heterogeneities in adhesive complexes, which exist as puncta along the junction.<sup>38</sup> For example, lower junctional E-cadherin levels spatially orient medioapical contractile flows to coordinate junction contractions.<sup>39</sup> These domains' potential for RhoA activation can be exacerbated by the junctional landscape. The local junction composition, specifically lipid and other protein signaling, could generate these distinct contractile units. Indeed, lifetimes of active GTP-RhoA can be enhanced via a coincidence detection scheme upon cyclic binding to the lipid PIP<sub>2</sub> and the junctional protein Anillin.<sup>26</sup> Protein-lipid microdomains, scattered along the junction, could therefore create a permissive environment for RhoA activation that is necessary for junction contractions. Spatial heterogeneities in adhesion, lipids, and protein localization could therefore be critical in determining which portion of the junction is capable of activating RhoA. Further work is needed to discern what specifies these unique microdomains.

These data have serious implications for the canonical mathematical models of epithelial tissues. In traditional vertex models, the tissue is a network of edges and nodes whose geometry and topology depends on active forces. The positions of these vertices anchoring bicellular interfaces are determined by the parameters of interfacial tension and pressure within each cell.<sup>35</sup> Vertices can then move in response to mechanical forces, but the extent of this movement is proportional to the parameters describing vertex friction, shoulder edge tension, and tricellular contact stiffness. Using our heterogeneous junction model, no one single parameter describing friction, tension, or stiffness was able to recapitulate experimental data. Instead, we find that the incorporation increases in friction arising from local RhoA activation successfully modeled vertex asymmetry.

Most studies of cell shape changes, to date, concern the movement of bicellular interfaces between two neighboring cells. In development, these junctional zones experience spatially distinct contractile flows that drive qualitatively different and rather opposing junctional responses. Medioapical flows to the bicellular region correspond to junction deformations, whereas flows to the tricellular contacts restrict such contractions.<sup>5,13</sup> We see similar junctional responses by optogenetically activating specific junctional zones, with the region of RhoA activation accumulating E-cadherin. Our previous work examining stable junction deformations show that longer optogenetic activations facilitate junction length changes through E-cadherin clustering and internalization.<sup>9</sup> It would be of interest to see how optogenetic activation of these junctional zones at longer timescales would facilitate their remodeling.

Yet, what is the physiological benefit in restricting vertex motion? In the *Drosophila* germband, tricellular E-cadherin recruitment is associated with the stabilization of the junctional ratchet. This stabilization ensures progressive interface shortening to facilitate cellular rearrangements.<sup>13</sup> In our optogenetic system, we do not find stable, irreversible contractions at short timescales but rather reversible junctional deformations. As such, it is unlikely that this vertex reinforcement is sufficient to stabilize junctional shortening. However, it may be necessary to maintain epithelial cohesion under increased tension of neighboring cells. Strong contractions, in principle, could compromise intercellular junctions and barrier functions. Indeed, vertices are principal sites of epithelial fracture in highly tensile epithelia.<sup>37</sup> Mechanosensitive reinforcement of vertices could therefore restrict major cell and tissue deformations to maintain tissue homeostasis. This mechanism seems plausible, as RhoA-mediated junctional mechanotransduction is a known regulator of tissue integrity.<sup>37</sup>

## STAR★METHODS

Detailed methods are provided in the online version of this paper and include the following:

- [KEY RESOURCES TABLE](#)
- [RESOURCE AVAILABILITY](#)
  - Lead contact
  - Materials availability
  - Data and code availability
- [EXPERIMENTAL MODEL AND SUBJECT DETAILS](#)
  - Cell lines
- [METHOD DETAILS](#)
  - Live-cell imaging and transfection
  - Drug treatments
  - qPCR
  - Immunofluorescence
  - Microscopy
  - Junction contraction and vertex displacement
  - Calculating HECD1 Intensities
  - Quantification of focal adhesion size
  - Contractile uniformity and center calculations
  - Computational model
  - Model parameters
  - Shoulder stiffness calculations
- [QUANTIFICATION AND STATISTICAL ANALYSIS](#)

## SUPPLEMENTAL INFORMATION

Supplemental information can be found online at <https://doi.org/10.1016/j.cub.2022.03.024>.

## ACKNOWLEDGMENTS

K.E.C. acknowledges an HHMI Gilliam Fellowship, National Academies of Sciences Ford Foundation Fellowship, and NIH training grant GM007183. M.L.G. acknowledges funding from NIH R01 GM104032. M.F.S. is supported by an EPSRC-funded PhD studentship. S. Banerjee acknowledges funding from NIH R35 GM143042, the Royal Society (URF/R1/180187), and HFSP (RGY0073/2018). S. Budnar and A.S.Y. were supported by grants and fellowships from NHMRC Australia (GNT1123816, 1164462, Fellowship 1136592) and the Australian Research Council (DP19010287).

**AUTHOR CONTRIBUTIONS**

Conceptualization, K.E.C., M.L.G., M.F.S., and S. Banerjee; methodology, K.E.C. and M.L.G.; experimental methodology, M.F.S. and S. Budnar; modeling methodology, S. Budnar and A.S.Y.; software, M.F.S. and S. Banerjee; formal analysis, K.E.C., M.F.S., and T.A.C.; investigation, K.E.C. and R.H.; resources, S. Budnar and A.S.Y.; writing – original draft, K.E.C. and M.F.S.; writing – review & editing, K.E.C., M.F.S., S. Banerjee, M.L.G., and T.A.C.; visualization, K.E.C. and M.F.S.; supervision, M.L.G. and S. Banerjee; funding acquisition, M.L.G. and S. Banerjee.

**DECLARATION OF INTERESTS**

The authors declare no competing interests.

Received: April 7, 2021

Revised: January 4, 2022

Accepted: March 8, 2022

Published: April 4, 2022

**REFERENCES**

1. Lecuit, T., Lenne, P.-F., and Munro, E. (2011). Force generation, transmission, and integration during cell and tissue morphogenesis. *Annu. Rev. Cell Dev. Biol.* 27, 157–184.
2. Fernandez-Gonzalez, R., and Zallen, J.A. (2011). Oscillatory behaviors and hierarchical assembly of contractile structures in intercalating cells. *Phys. Biol.* 8, 045005.
3. Jewett, C.E., Vanderleest, T.E., Miao, H., Xie, Y., Madhu, R., Loerke, D., and Blankenship, J.T. (2017). Planar polarized Rab35 functions as an oscillatory ratchet during cell intercalation in the *Drosophila* epithelium. *Nat. Commun.* 8, 476.
4. Mason, F.M., Tworoger, M., and Martin, A.C. (2013). Apical domain polarization localizes actin–myosin activity to drive ratchet-like apical constriction. *Nat. Cell Biol.* 15, 926–936.
5. Rauzi, M., Lenne, P.-F., and Lecuit, T. (2010). Planar polarized actomyosin contractile flows control epithelial junction remodelling. *Nature* 468, 1110–1114.
6. Solon, J., Kaya-Çopur, A., Colombelli, J., and Brunner, D. (2009). Pulsed forces timed by a ratchet-like mechanism drive directed tissue movement during dorsal closure. *Cell* 137, 1331–1342.
7. Kerridge, S., Munjal, A., Philippe, J.-M., Jha, A., de las Bayonas, A.G., Saurin, A.J., and Lecuit, T. (2016). Modular activation of Rho1 by GPCR signalling imparts polarized myosin II activation during morphogenesis. *Nat. Cell Biol.* 18, 261–270.
8. Munjal, A., Philippe, J.-M., Munro, E., and Lecuit, T. (2015). A self-organized biomechanical network drives shape changes during tissue morphogenesis. *Nature* 524, 351–355.
9. Cavanaugh, K.E., Staddon, M.F., Munro, E., Banerjee, S., and Gardel, M.L. (2020). RhoA mediates epithelial cell shape changes via mechanosensitive endocytosis. *Dev. Cell* 52, 152–166.e5.
10. Staddon, M.F., Cavanaugh, K.E., Munro, E.M., Gardel, M.L., and Banerjee, S. (2019). Mechanosensitive junction remodeling promotes robust epithelial morphogenesis. *Biophys. J.* 117, 1739–1750.
11. García-Mata, R., and Burridge, K. (2007). Catching a GEF by its tail. *Trends Cell Biol.* 17, 36–43.
12. Mason, F.M., Xie, S., Vasquez, C.G., Tworoger, M., and Martin, A.C. (2016). RhoA GTPase inhibition organizes contraction during epithelial morphogenesis. *J. Cell Biol.* 214, 603–617.
13. Vanderleest, T.E., Smits, C.M., Xie, Y., Jewett, C.E., Blankenship, J.T., and Loerke, D. (2018). Vertex sliding drives intercalation by radial coupling of adhesion and actomyosin networks during *Drosophila* germband extension. *eLife* 7, e34586.
14. Huebner, R.J., Malmi-Kakkada, A.N., Sarikaya, S., Weng, S., Thirumalai, D., and Wallingford, J.B. (2021). Mechanical heterogeneity along single-cell-cell junctions is driven by lateral clustering of cadherins during vertebrate axis elongation. *Elife* 10, e65390.
15. Choi, W., Acharya, B.R., Peyret, G., Fardin, M.-A., Mège, R.-M., Ladoux, B., Yap, A.S., Fanning, A.S., and Peifer, M. (2016). Remodeling the zonula adherens in response to tension and the role of afadin in this response. *J. Cell Biol.* 213, 243–260.
16. Acharya, B.R., Wu, S.K., Lieu, Z.Z., Parton, R.G., Grill, S.W., Bershadsky, A.D., Gomez, G.A., and Yap, A.S. (2017). Mammalian diaphanous 1 mediates a pathway for E-cadherin to stabilize epithelial barriers through junctional contractility. *Cell Rep.* 18, 2854–2867.
17. Manibog, K., Li, H., Rakshit, S., and Sivasankar, S. (2014). Resolving the molecular mechanism of cadherin catch bond formation. *Nat. Commun.* 5, 3941.
18. Buckley, C.D., Tan, J., Anderson, K.L., Hanein, D., Volkmann, N., Weis, W.I., Nelson, W.J., and Dunn, A.R. (2014). Cell adhesion. The minimal cadherin–catenin complex binds to actin filaments under force. *Science* 346, 1254211.
19. Hong, S., Troyanovsky, R.B., and Troyanovsky, S.M. (2013). Binding to F-actin guides cadherin cluster assembly, stability, and movement. *J. Cell Biol.* 201, 131–143.
20. Pannekoek, W.-J., de Rooij, J., and Grootenhuis, M. (2019). Force transduction by cadherin adhesions in morphogenesis. *F1000Res* 8, 1044.
21. Liang, X., Budnar, S., Gupta, S., Verma, S., Han, S.-P., Hill, M.M., Daly, R.J., Parton, R.G., Hamilton, N.A., Gomez, G.A., and Yap, A.S. (2017). Tyrosine dephosphorylated cortactin downregulates contractility at the epithelial zonula adherens through SRGAP1. *Nat. Commun.* 8, 790.
22. Oakes, P.W., Wagner, E., Brand, C.A., Probst, D., Linke, M., Schwarz, U.S., Glotzer, M., and Gardel, M.L. (2017). Optogenetic control of RhoA reveals zyxin-mediated elasticity of stress fibres. *Nat. Commun.* 8, 15817.
23. Strickland, D., Lin, Y., Wagner, E., Hope, C.M., Zayner, J., Antoniou, C., Sosnick, T.R., Weiss, E.L., and Glotzer, M. (2012). TULIPs: tunable, light-controlled interacting protein tags for cell biology. *Nat. Methods* 9, 379–384.
24. Wagner, E., and Glotzer, M. (2016). Local RhoA activation induces cytokinetic furrows independent of spindle position and cell cycle stage. *J. Cell Biol.* 213, 641–649.
25. Piekny, A.J., and Glotzer, M. (2008). Anillin is a scaffold protein that links RhoA, actin, and myosin during cytokinesis. *Curr. Biol.* 18, 30–36.
26. Budnar, S., Husain, K.B., Gomez, G.A., Naghibosadat, M., Varma, A., Verma, S., Hamilton, N.A., Morris, R.G., and Yap, A.S. (2019). Anillin promotes cell contractility by cyclic resetting of RhoA residence kinetics. *Dev. Cell* 49, 894–906.e12.
27. Levayer, R., Pelissier-Monier, A., and Lecuit, T. (2011). Spatial regulation of Dia and myosin-II by RhoGEF2 controls initiation of E-cadherin endocytosis during epithelial morphogenesis. *Nat. Cell Biol.* 13, 529–540.
28. Stoops, S.L., Pearson, A.S., Weaver, C., Waterson, A.G., Days, E., Farmer, C., Brady, S., Weaver, C.D., Beauchamp, R.D., and Lindsley, C.W. (2011). Identification and optimization of small molecules that restore E-cadherin expression and reduce invasion in colorectal carcinoma cells. *ACS Chem. Biol.* 6, 452–465.
29. Iyer, K.V., Piscitello-Gómez, R., Paijmans, J., Jülicher, F., and Eaton, S. (2019). Epithelial viscoelasticity is regulated by mechanosensitive E-cadherin turnover. *Curr. Biol.* 29, 578–591.e5.
30. Noordstra, I., Díez Hermoso, M., Schimmel, L., Bonfim-Melo, A., Kalappurakkal, J.M., Mayor, S., Gordon, E., Roca Cusachs, P., and Yap, A.S. (2021). Cortical actin flow activates an  $\alpha$ -catenin clutch to assemble adherens junctions. Preprint at bioRxiv. <https://doi.org/10.1101/2021.07.28.454239>.
31. Gardel, M.L., Schneider, I.C., Aratyn-Schaus, Y., and Waterman, C.M. (2010). Mechanical integration of actin and adhesion dynamics in cell migration. *Annu. Rev. Cell Dev. Biol.* 26, 315–333.
32. Aratyn-Schaus, Y., and Gardel, M.L. (2010). Transient frictional slip between integrin and the ECM in focal adhesions under myosin II tension. *Curr. Biol.* 20, 1145–1153.

33. Alt, S., Ganguly, P., and Salbreux, G. (2017). Vertex models: from cell mechanics to tissue morphogenesis. *Philos. Trans. R. Soc. Lond. B Biol. Sci.* **372**, 28348254.
34. Farhadifar, R., Röper, J.-C., Aigouy, B., Eaton, S., and Jülicher, F. (2007). The influence of cell mechanics, cell-cell interactions, and proliferation on epithelial packing. *Curr. Biol.* **17**, 2095–2104.
35. Fletcher, A.G., Osterfield, M., Baker, R.E., and Shvartsman, S.Y. (2014). Vertex models of epithelial morphogenesis. *Biophys. J.* **106**, 2291–2304.
36. Noll, N., Streichan, S.J., and Shraiman, B.I. (2020). Geometry of epithelial cells provides a robust method for image based inference of stress within tissues. *Phys. Rev. X* **10**, 011072.
37. Acharya, B.R., Nestor-Bergmann, A., Liang, X., Gupta, S., Duszyc, K., Gauquelin, E., Gomez, G.A., Budnar, S., Marcq, P., Jensen, O.E., et al. (2018). A mechanosensitive RhoA pathway that protects epithelia against acute tensile stress. *Dev. Cell* **47**, 439–452.e6.
38. Cavey, M., Rauzi, M., Lenne, P.-F., and Lecuit, T. (2008). A two-tiered mechanism for stabilization and immobilization of E-cadherin. *Nature* **453**, 751–756.
39. Levayer, R., and Lecuit, T. (2013). Oscillation and polarity of E-cadherin asymmetries control actomyosin flow patterns during morphogenesis. *Dev. Cell* **26**, 162–175.
40. Schneider, C.A., Rasband, W.S., and Eliceiri, K.W. (2012). NIH Image to ImageJ: 25 years of image analysis. *Nat. Methods* **9**, 671–675.
41. Cavanaugh, K.E., Oakes, P.W., and Gardel, M.L. (2020). Optogenetic control of RhoA to probe subcellular mechanochemical circuitry. *Curr. Protoc. Cell Biol.* **86**, e102.
42. Huang, J.X., Lee, G., Cavanaugh, K.E., Chang, J.W., Gardel, M.L., and Moellering, R.E. (2019). High throughput discovery of functional protein modifications by hotspot thermal profiling. *Nat. Methods* **16**, 894–901.
43. Hartigan, J.A., and Hartigan, P.M. (1985). The dip test of unimodality. *Ann. Statist.* **13**, 70–84.

**STAR★METHODS**

**KEY RESOURCES TABLE**

REAGENT or RESOURCE	SOURCE	IDENTIFIER
<b>Antibodies</b>		
Anti-E-Cadherin HECD1	Abcam	Ab1416; RRID:AB_300946
Anti-E-Cadherin DECMA	Abcam	Ab11512; RRID:AB_298118
Alexa Fluor Goat anti Mouse 647	Invitrogen	Cat#A-21235; RRID: AB_2535804
Alexa Fluor Goat anti Rat 647	Invitrogen	Cat#A-21247; RRID:AB_141778
Paxillin (5H11)	Millipore	Cat#05-417; RRID:AB_309724
Alexa Fluor 488 Phalloidin	ThermoFisher	Cat#A12379
<b>Bacterial and virus strains</b>		
Stellar Competent E. coli	Clontech	Cat#636766
<b>Chemicals, peptides, and recombinant proteins</b>		
C3 Transferase	Cytoskeleton, inc.	Cat#CT04
CN03	Cytoskeleton, inc.	Cat#CN03
Lipofectamine 3000	Invitrogen	Cat#L3000015
ResEcad	Sigma-Aldrich	Cat#205615
NSC23766	Tocris	Cat#2161
<b>Critical commercial assays</b>		
NucleoSpin RNA Purification Kit	Macherey Nagel	Cat#740955
SuperScript III System	Invitrogen	Cat#18080051
PrimeTime Gene Expression Master Mix	IDT	Cat#1055772
<b>Experimental models: Cell lines</b>		
Human: Caco-2 2xPDZ-LARG; Stargazin-LOVpep	Cavanaugh et al. <sup>9</sup>	N/A
Human: Caco-2 E-Cadherin GFP	Acharya et al. <sup>16</sup>	N/A
Human: Caco-2	ATCC	HTB-37
<b>Oligonucleotides</b>		
CDH1 (Hs.PT.58.33240271)	IDT	N/A
GAPDH (Hs.PT.39a.22214836)	IDT	N/A
<b>Recombinant DNA</b>		
mCherry-APH	Budnar et al. <sup>26</sup>	N/A
<b>Software and algorithms</b>		
FIJI	Schneider et al. <sup>40</sup>	Fiji.sc
Snapgene Software	GSL Biotech LLC	Snapgene.com
Metamorph	Molecular Devices	Moleculardevices.com
Prism	GraphPad Software	Graphpad.com
Excel	Microsoft	Microsoft.com
Matlab	MathWorks	Mathworks.com
Python	Python	Python.org
<b>Other</b>		
Nunc Lab Tek II Chamber Slides	ThermoFisher	Cat#155453PK
Ibidi 4-well Chamber	Ibidi	Cat\$80426
Rat Tail Collagen I	Corning	Cat#354236
ProLong Gold	ThermoFisher	Cat#10144

## RESOURCE AVAILABILITY

### Lead contact

Further information and reagent requests should be directed to the lead contact, Margaret Gardel ([gardel@uchicago.edu](mailto:gardel@uchicago.edu)).

### Materials availability

This study did not generate new unique reagents. All reagents in this study are available from the [lead contact](#) with a completed Materials Transfer Agreement upon request.

### Data and code availability

- All data reported in this paper will be shared by the [lead contact](#) upon request.
- Code will be available at <https://github.com/BanerjeeLab/CellJunctionModel>
- Any additional information required to reanalyze the data reported in this paper is available from the [lead contact](#) upon request.

## EXPERIMENTAL MODEL AND SUBJECT DETAILS

### Cell lines

Male Colorectal adenocarcinoma cells (Caco-2) with genetic backgrounds of WT, E-Cadherin-GFP CRISPR (generated in<sup>16</sup>), and optogenetic lines (generated in<sup>9</sup>) were cultured in DMEM media (Corning), and supplemented with 5% Fetal Bovine Serum (Corning), 2 mM L-glutamine (Corning), and penicillin-streptomycin (Corning). Cell lines were maintained in a humidified incubator at 37C with 5% CO<sub>2</sub>.

## METHOD DETAILS

### Live-cell imaging and transfection

To ensure a confluent and mature epithelial monolayer, Caco-2 cells were plated densely on 2 μ m/ml polymerized collagen gels<sup>9,41</sup> (unless specified otherwise) coating the bottom of a 4-well Ibidi Chamber (Ibidi). Cells were then allowed to grow for at least 1-2 days to ensure a polarized and confluent monolayer. Ibidi chambers were then placed into a stage incubator with temperature, humidity, and CO<sub>2</sub> control (Chamlide TC and FC-5N; Quorum Technologies). All pieces of the stage incubator (stage, adapter, cover, and objective) were maintained at 37C. To analyze RhoA dynamics, 5 μ g of mCherry-AHPH RhoA biosensor DNA was transfected into GFP E-cadherin CRISPR cells using Lipofectamine 3000 (Invitrogen) at least 24 hours before imaging. For CN03 wash-in experiments, cells were imaged in the 488 and 561 channels every 5 or 8 minutes, until 2 hours of timelapse imaging was completed. At the beginning of imaging, either media or 1 μ g/ml CN03 was added to the media to document junctional responses. To visualize E-Cadherin in the optogenetic system, we bathed the cells in HECD1 (Abcam) primary and secondary antibody, Alexa Fluor goat Anti-Mouse 647 (Invitrogen), both at a 1:1500 dilution in normal media for at least 24 hours. When applicable, E-cadherin was visualized using DECMA (Abcam) primary and secondary Alexa Fluor Goat Anti-Rat (Invitrogen) antibodies at 1:1500 dilution in normal media for at least 24 hours. Before imaging, cells were washed with PBS and replaced with normal media or media containing chemical perturbations described below. For optogenetic experiments, cells were imaged in the 561 and 647 channel every 35 seconds. The first 10 minutes was to establish a baseline junctional response before the 5-minute optogenetic activation, with the last 15 minutes documenting junctional relaxation. During the activation period, a region around the junction was manually drawn in MetaMorph and adjusted in real time for illumination by the 405nm laser for 1000ms immediately before the acquisition of each image. Laser power was at 1000AU. For junction and vertex movement analysis, via both CN03 and optogenetic means, we chose to analyze junctions that were distal from cell divisions and/or apoptotic extruding cells to ensure a cohesive monolayer. For picking optogenetic cells, cells were chosen based off of their expression level, which showed junctional recruitment and depletion of the prGEF from the cytosol. All junctions were imaged at the apical plane just below the surface to visualize all vertices and junctional connections.

### Drug treatments

Cells were treated with a 1:1500 dilution DECMA antibody treatment 24 hours before experimentation. Optogenetic and WT cells were treated with 500 μ M ResEcad (Calbiochem) or 100 μ M NSC23766 (Tocris) 24-48 hours before optogenetic activation or downstream applications such as fix-and-stains or qPCR.

### qPCR

Total RNA was isolated with NucleoSpin kits (Macherey-Nagel). First-strand synthesis was carried out using the SuperScript III system (Invitrogen) with an oligo dT primer and 200 ng of total RNA as input. First-strand reactions were diluted 5-fold and 2 μ l was used as template in 20 μ l reactions prepared with PrimeTime master mix (IDT) and PrimeTime pre-designed qPCR primer/probe mixtures from IDT (CDH1: Hs.PT.58.3324071; GAPDH: Hs.PT.39a.22214836). A StepOnePlus instrument (Applied Biosystems) was used for running the qPCR reactions. Relative mRNA levels were determined by the 2-ΔΔCt method utilizing GAPDH as a reference gene.

### Immunofluorescence

Cells were plated onto polymerized collagen gels coating a Lab Tek II Chamber slide (Thermo Fisher Scientific). Once a confluent monolayer was formed, cells were fixed with 4%PFA with 0.1% Triton X-100 in PBS solution (Corning). Permeabilization was achieved through 0.5% Triton X-100 for 10 min and then cells were blocked with 2.5% BSA and 0.1% Triton X-100 in PBS for one hour. Primary antibody, Paxillin (Millipore) at 1:300 or HECD1 at 1:300, was incubated in blocking solution overnight at 4C and then washed at least 3 times for 20 minutes in 0.1% Triton X-100. Slides were then coated with secondary antibody, Alexa Fluor Goat anti-Mouse 647 (Invitrogen), and Alexa Fluor phalloidin 488 (ThermoFisher) in blocking solution for one hour. After 3 consecutive 20-minute washes in 0.1% Triton X-100, slide chambers were removed and coated with 20ul ProLong Gold (ThermoFisher Scientific). Slides were then sealed with glass coverslips before drying and sealing with nail polish. Slides were then stored at 4C.

### Microscopy

Optogenetic experiments were performed on an inverted Nikon T-E (Nikon, Melville, NY) with a laser merge module with 491, 561, and 642nm laser lines (Spectral Applied Research, Ontario, Canada) with a Yokogawa CSU-X confocal scanning head (Yokogawa Electric, Tokyo, Japan). The Zyla 4.2 sCMOS Camera (Andor, Belfast, UK) collected the images. Optogenetic activation was achieved using a Mosaic digital micromirror device (Andor) attached to a 405nm laser. Images were collected on a 60X 1.2 Plan Apo water (Nikon) objective. MetaMorph Automation and Image Analysis Software (Molecular Devices, Sunnyvale, CA) controlled all hardware. Fix-and-stain and live-cell imaging of CN03 wash-ins were performed on an LSM 980 system with an Airyscan 2 (Zeiss) detector in super resolution-mode with a 63x NA1.4 oil objective (Zeiss). Microscopy software used was the Zen digital imaging suite (Zeiss).

### Junction contraction and vertex displacement

Vertex displacement and individual vertex traces were acquired by manually tracking each vertex in a vertex pair using the Manual Tracking tool in Fiji<sup>40</sup>. Junction lengths were analyzed by manually measuring in each frame the junction length using the free hand line tool in FIJI software. Junction kymographs were generated with a python script written in FIJI to reconstruct user-drawn line segments along the junction proper. Kymographs were made from unregistered image stacks to preserve asymmetry in junction contraction. Linescans of activated regions and E-cadherin along the junction were taken using the Plot Profile tool of a hand-drawn line along the junction in FIJI. Linescans were taken before optogenetic activation and after 5 minutes of activation. Junction intensity profiles were then normalized for the junction length from 0 to 1. Contracted length was calculated by dividing the length of the junction at T=5 divided by the length at T=0 during optogenetic activation. Percent movement was calculated as the displacement of each vertex from the original vertex position in a kymograph divided by the sum of both vertex displacements.

### Calculating HECD1 Intensities

Vertex fluorescence HECD1 intensities were calculated by drawing a circle around the vertex region in each frame and measuring the intensities over the time course using the FIJI intensity analysis tool. HECD1 fluorescence intensities over time for center-third activations were measured by taking the outline of the activation mask and measuring intensities within that region of activation with the FIJI measure tool. To analyze a region distal to the region of activation, the mask was once again used as a reference length but manually adjusted to exclude tricellular vertices and the activation region.

### Quantification of focal adhesion size

To analyze focal adhesion size and number, the paxillin channel was thresholded and made into a binary mask to calculate the area of focal adhesions within a cell, as indicated by boundary edges seen from apical actin staining, as performed in Huang et al<sup>42</sup>. The binary mask was then overlaid onto the paxillin channel to segment the image and calculate the area of paxillin with a threshold of 0.25  $\mu\text{m}^2$  and also the number of focal adhesions within that cellular region identified by apical actin staining.

### Contractile uniformity and center calculations

Contractile uniformity within each junction was analyzed by manually tracking E-cadherin puncta in each kymograph using the paint-brush tool in FIJI. Both the displacement and position along the junction were normalized by the initial junction length, and set so that the less-motile vertex has position 0 and the motile vertex has position 1. The maximal displacement of each contracting E-cad puncta as a function of the initial position along the junction was found. The data was then binned by normalized junction position, and the mean and standard deviation plotted (Figure 2B). The kymograph's center of contraction was determined by the root value of the linear fit through a graph of vertex displacement vs average distance from junction center, and the center of contraction was then normalized so that the position of the less-motile vertex was 0 and the more motile vertex as 1, meaning the center of the junction would be the position of 0.5. RhoA localization along the junction was found by averaging the AHPH RhoA intensity at the final five timepoints within the kymograph and fitting it to a gaussian using the Matlab fit function. The junction position of the gaussian peak was determined to be the center of RhoA localization and normalized.

### Computational model

The junction is model by an elastic continuum with Young's modulus  $E$ , RhoA induced contractility  $A(x)$  and friction  $\mu(x)$ , which may both vary along the junction. The shoulder junctions are modelled as provided a simple spring like resistance to deformation, with stiffnesses  $k_{bot}$  and  $k_{top}$  at the ends of the junction. We normalize space by the length of the junction, such that  $x=0$  and  $x=1$ .

are the locations of the vertices, and we normalize stresses by the Young's modulus of the junction, such that  $E = 1$ , leaving us only with dimensions in time.

To numerically solve the model for the junction, we discretize the system into  $n$  equally spaced points along the junction,  $u_i$ , with tension  $\lambda_i$  and friction coefficient  $\mu_i$ . The discretized equations of motion are given by:

$$\mu_0 \dot{u}_1 = \frac{E(u_2 - u_1 - dx)}{dx} + \lambda_0 - k_{bot} u_2,$$

$$\mu_i \dot{u}_i = \frac{E(u_{i+1} - 2u_i + u_{i-1})}{dx^2} + \frac{(\lambda_{i+1} - \lambda_{i-1})}{2dx}, \text{ for } i=2, \dots, n-1$$

$$\mu_n \dot{u}_n = \frac{E(u_n - u_{n-1} - dx)}{dx} - \lambda_n - k_{top}(u_n - 1),$$

where  $dx = (1/n)$  is the distance between position along the junction. The equations are then integrated numerically over time using the python package `scipy`. For each set of simulations, 100 samples are taken.

### Model parameters

The model parameters are obtained by analyzing the average vertex motion over time. We observed that vertex motion slows with time, and thus slows with displacement. Assuming a simple linear spring model  $\dot{u} = (\Lambda - (k+E)u)/\mu$ , we can fit the speed vs displacement curve with a straight line to obtain the tension to friction ratio  $\Lambda_0/\mu_0$  from the intercept, and relative stiffness,  $(k_0+E)/\mu_0$ , from the slope. Since our parameter values are relative, we may estimate these values by choosing tension  $\Lambda_0 = 1.5$ , and Young's modulus  $E = 1$ .

Parameter	Symbol	Value
Number of points	$n$	21
Junction Young's Modulus	$E$	1
Tension	$\Lambda_0$	1.5
Friction Coefficient	$\mu_0$	40.1 min
Shoulder stiffness	$k_0$	4.52

Next, we analyze the motion of the motile and less-motile vertices separately. We find that the motile vertex has a lower relative friction, as it initially moves faster, a lower relative stiffness, as it slows less with displacement, than the less-motile vertex. However, from the RhoA profiles we observe roughly twice as much RhoA at the less-motile vertex than the motile vertex. Thus, using our fit values and assuming a motile tension of  $\Lambda_M = 1$  and less-motile tension  $\Lambda_{LM} = 2$ , we obtain values for the stiffness,  $k_M$  and  $k_{LM}$ , and the friction,  $\mu_M$  and  $\mu_{LM}$ , at the motile and less-motile vertices. Finally, to introduce coupling between force and adhesion strength and elastic stiffness into the model, we set the friction and stiffness to be exponential functions of the tension that match our deduced values at  $\Lambda = 1$  and  $\Lambda = 2$ :

$$\mu(\Lambda) = \mu_M \left( \frac{\mu_{LM}}{\mu_M} \right)^{\Lambda-1},$$

and

$$k(\Lambda) = k_M \left( \frac{k_{LM}}{k_M} \right)^{\Lambda-1}.$$

Tension is then sampled from a normal distribution at each vertex with mean 1.5 and standard deviation 0.5. The parameters obtained are listed below:

Parameter	Symbol	Value
Number of points	$n$	21
Junction Young's Modulus	$E$	1
Motile Tension	$\Lambda_M$	1
Less-Motile Tension	$\Lambda_{LM}$	2
Motile Friction Coefficient	$\mu_M$	20.3 min
Less-Motile Friction Coefficient	$\mu_{LM}$	77.3 min

(Continued on next page)

**Continued**

Parameter	Symbol	Value
Motile Shoulder stiffness	$k_M$	0.996
Less-Motile Shoulder stiffness	$k_{LM}$	17.5

### Shoulder stiffness calculations

To estimate the mechanical resistance to motion from the shoulder junctions, we use a simple line tension model of the junctions. Assuming that line tension from the junctions is under force balance, we may calculate the relative tensions from the force balance and derive an effective mechanical energy of the system as the central junction changes length. From this, the second derivative gives us the mechanical stiffness from the shoulder junctions. Let  $\lambda$  be the tension of the central junction,  $\lambda_1$  and  $\lambda_2$  the tensions of the two shoulder junctions, and  $\theta_1$  and  $\theta_2$  be the angles between the shoulder junctions and the central junction, and  $l_1$  and  $l_2$  be the initial shoulder junction lengths.

By force balance we have:

$$\lambda_1 \sin \theta_1 = \lambda_2 \sin \sin \theta_2$$

and

$$\lambda = \lambda_1 \cos \cos \theta_1 + \lambda_2 \cos \cos \theta_2$$

in the x and y directions, respectively, which give the relative tensions.

Next, we calculate the effective resistance from the shoulders by considering the second derivative of the energy with respect to the junction length,  $y$ . We can write the shoulder junction lengths as

$$L_i(y) = (l_i^2 \theta_i + y^2)^{\frac{1}{2}},$$

with first derivative

$$\frac{dL_i}{dy} = \frac{y}{L_i},$$

and second derivative

$$\frac{d^2L_i}{dy^2} = \frac{\theta_i}{L_i}.$$

Thus, the mechanical energy  $E = \lambda_1 L_1 + \lambda_2 L_2 - \lambda y$  has second derivative at the initial position of  $d^2E/dy^2 = (\lambda_1 \theta_1 / l_1) + (\lambda_2 \theta_2 / l_2) = k$  the effective shoulder stiffness.

### QUANTIFICATION AND STATISTICAL ANALYSIS

Statistical analysis was performed in Excel, GraphPad Prism, and Matlab, to establish statistical significance under specific experimental conditions. Where applicable, boxes indicate Standard Deviation and whiskers indicate Standard Error. Normally distributed data were analyzed for significance with \*\*\*\*=p<0.0001, \*\*\*=p<0.0009, and \*\*=p<0.05 as calculated by the two-tailed Student's t-Test. Bimodal data was calculated for significance using a Hartigan Dip Test<sup>43</sup>. n represents the number of junctions or vertices analyzed in each experiment, which is indicated in the figure and its respective legend. Data was only excluded if the optogenetically activated junction was proximal to a cell division event and/or extruding cell because this mechanical perturbation affected local junctional mechanics within the analyzed tissue area.